Chapter 1
Numerical Experiment of Stratification Induced by Diurnal Solar Heating Over the Louisiana Shelf

Mohammad Nabi Allahdadi and Chunyan Li

Abstract The effect of diurnal solar heating on the stratification of waters over the Louisiana shelf was examined using the 3-dimensional Finite Volume Community Ocean Model (FVCOM). The simulation was for June 2009 to examine the effects of solar heating on summertime stratification. The input components of solar radiation to the FVCOM model were calculated using available relationships for shortwave, longwave, latent heat, and sensible heat radiation and using Metocean field data obtained from WAVCIS stations. Simulation results showed a continuous increase in water temperature and stratification during June 2009 with daily fluctuations of sea surface temperature as large as 0.9 °C. The corresponding stratification strengthening was quantified by an increase in the gradient Richardson number and buoyancy frequency. Development of shelf-wide stratification coincided with a significant decline in bottom water oxygen concentration. Our results demonstrate how, under certain conditions, solar heating can significantly contribute to vertical stratification and may also create conditions conducive to the formation and persistence of hypoxia.

Keywords Numerical modeling · Solar radiation · Stratification · Hypoxia · FVCOM · Louisiana shelf · Gulf of Mexico

M.N. Allahdadi (✉)
Department of Marine, Earth and Atmospheric Sciences,
North Carolina State University, Raleigh, USA
e-mail: nabiallahdadi@gmail.com

C. Li
Department of Oceanography and Coastal Sciences, Coastal Studies Institute,
Louisiana State University, Baton Rouge, USA
e-mail: cli@lsu.edu

D. Justic et al. (eds.), *Modeling Coastal Hypoxia*,
DOI 10.1007/978-3-319-54571-4_1

1.1 Background

Hypoxia is a condition of low dissolved oxygen concentration less than 2 mg/l (Rabalais et al. 2002). Over the Texas–Louisiana shelf, hypoxia is a seasonal phenomenon that starts in late spring or early summer and persists in bottom waters until the early fall (Wiseman et al. 1997). The seasonal occurrence of hypoxia is the result of influence from several biological and physical factors. The springtime floods of the Mississippi and the Atchafalaya rivers greatly increase nutrient loadings to the shelf area (Wiseman et al. 1997). Biological processes supported by this increased nutrient load contribute to oxygen depletion in bottom waters, thereby producing hypoxia 1–2 months after the peak in river discharge (Justic et al. 1996). Freshwater associated with river flooding also increases the buoyancy of shelf waters and thereby strengthens the stratification, which allows for the hypoxia formation (Wiseman et al. 1997). However, a significant portion of stratification can be induced by solar heating during summertime and can act as primary contributing factor to seasonal hypoxia development in the northern Gulf of Mexico (Hagy and Murrell 2007). The role of water column mixing in re-oxygenating bottom waters and mitigating hypoxic events, as well as the positive feedback between stratification and hypoxia and its role in mediating pollutant distribution, have been addressed by several studies for the Texas–Louisiana shelf (Wiseman et al. 1997; Wang and Justic 2009; Allahdadi et al. 2013; Chaichitehrani 2012; Tehrani et al. 2013). Allahdadi et al. (2013) compared the relative Richardson numbers for stations located to the east and west of the Mississippi Delta and concluded that for the western stations, the Richardson numbers were an order of magnitude larger than those for the eastern stations.

Buoyancy is dependent on temperature and salinity gradients in the vertical dimension. Solar radiation increases in the beginning of the summer. This causes the water column to stratify with higher sea surface temperature. The stratification varies periodically due to diurnal variations of solar heat (Chen et al. 2003).

Increasing solar radiation has both positive and negative impacts on reducing bottom water oxygen. Although the stratification caused by excess solar heating inhibits bottom water re-oxygenation, it can also enhance photosynthesis and affect the balance between photosynthesis and respiration rate. In very shallow estuarine waters, where stratification is not dominant, hypoxic events generally correspond to low solar radiation. An example of such phenomenon is the hypoxic events in the Upper Newport Bay Estuary, California (water depth less than 5 m) that tended to occur more frequently on cloudy days (Nezlin et al. 2009). However, for the deeper shelf waters of Louisiana west of the Mississippi Delta, we expect that stratification is dominant and there is negative feedback between solar radiation and bottom water oxygen concentration.

Many studies have addressed different physical and biogeochemical causes of hypoxia over the Louisiana shelf (for example Justic et al. 2003, Rabalais and Louisiana Universities Marine Consortum 1991, Rabalais et al. 2004, Turner and

Rabalais 1994, Turner et al. 2008). However, the effect of summer solar heating on stratification and hypoxia formation has not been studied.

The present study examines the effects of solar radiation on stratification for the Louisiana shelf west of the Mississippi Delta using FVCOM simulations. The effect of solar heating on water column temperature is included as a heat source term in the model heat balance equation. The approach has been used by others to study the effect of atmospheric heat budget on the water column stratification and mixing (e.g., Elsberry et al. 1976; Price 1981; Bender et al. 1993; Zedler et al. 2002). We followed the approach of the Chen et al. (2003) here, who applied the ECOM-Si model with different components of radiation to study stratification and circulation over the Georges Bank in the Gulf of Maine. Determining parameters for the vertical structure of downward heat flux in the water column was a challenge in their study. They used the distinction between coastal and ocean waters to specify the attenuation of different wavelengths in the water column. They compared their simulated sea surface temperature (SST) with satellite-derived values, and their results showed a diurnal fluctuation of SST with approximately 1 °C difference between day and night temperatures superimposed on a general increasing trend. In the present study, we used the same approach with the FVCOM model.

1.2 Numerical Model

In order to study the effect of solar heating on shelf stratification, solar radiation components were introduced to an existing implementation of FVCOM (Fig. 1.1, Allahdadi 2015). FVCOM is a prognostic, unstructured grid, finite volume, free surface, three-dimensional (3-D) primitive equations ocean model (Chen et al. 2006). The main equations solved by the model are momentum, continuity, salt transport, heat transport, and density equation. The equations representing heat and salt transport and density contribution are as follows:

$$\frac{\partial T}{\partial t} + u\frac{\partial T}{\partial x} + v\frac{\partial T}{\partial y} + w\frac{\partial T}{\partial z} = \frac{\partial}{\partial z}\left(K_h\frac{\partial T}{\partial z}\right) + F_T \tag{1.1}$$

$$\frac{\partial S}{\partial t} + u\frac{\partial S}{\partial x} + v\frac{\partial S}{\partial y} + w\frac{\partial S}{\partial z} = \frac{\partial}{\partial z}\left(K_h\frac{\partial S}{\partial z}\right) + F_s \tag{1.2}$$

$$\rho = \rho(T, S) \tag{1.3}$$

where T is water temperature, S is salinity, and ρ is water density. u, v, and w are current velocity components in the horizontal (x and y), and vertical (z) directions. K_h is the coefficient of vertical diffusivity for salt and heat. F_T and F_s represent horizontal thermal and salt diffusion terms, respectively. Solar radiation is applied to the model equation through the surface boundary condition for temperature:

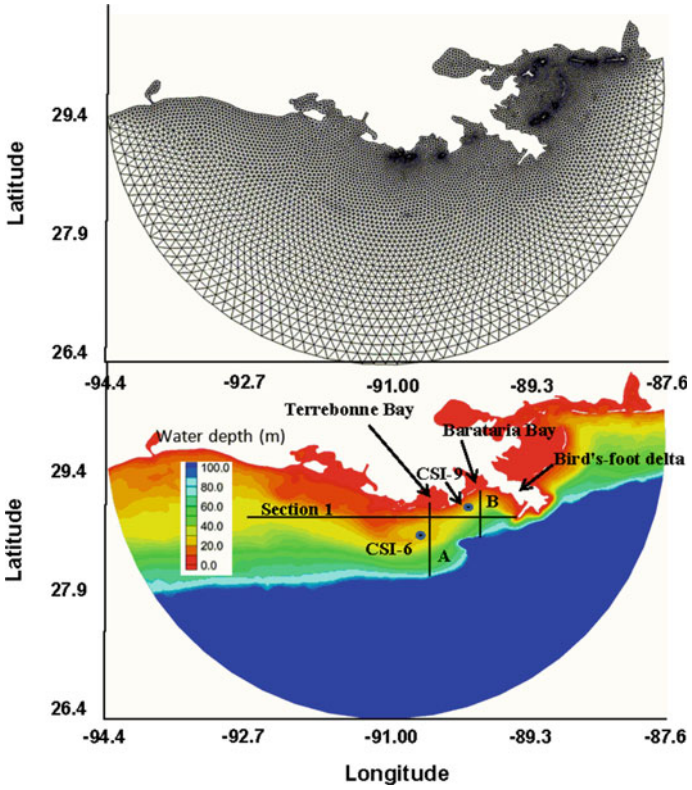

Fig. 1.1 Computational mesh and model bathymetry for the FVCOM model

$$\frac{\partial T}{\partial z} = \frac{1}{\rho c_p K_h}[Q_n(x,y,t) - SW(x,y,\xi,t)] \tag{1.4}$$

In the above equation, $Q_n(x,y,t)$ is the surface net heat flux that includes four components: shortwave flux, longwave flux, sensible heat flux, and latent heat flux. $SW(x,y,t)$ is the shortwave flux at sea surface, and C_p is the specific heat of seawater.

Governing equations of flow, and salt and heat transport, are discretized using finite volumes and solved with the Runge–Kutta method. Triangular grid elements are used for computation. This offers more flexibility, including islands and complicated coastline geometry that are common west of the Mississippi Delta. Furthermore, mesh flexibility allows finer spatial resolution where needed. For the present simulation, a region including the coastline from Mobile-AL to the west of the Sabine Bank, TX was used as the modeling area (Fig. 1.1). The model has a circular open boundary extended to the outer-shelf and deep water to the depths beyond 2000 m. Mesh resolution was the highest for the area associated with the inner-shelf west of the Mississippi Delta (about 500–1000 m, Fig. 1.1), which is

the area of focus in this study. This region includes the shallow shelf off Terrebonne Bay, outside of the Atchafalaya Bay, and outside of the Barataria Bay, whose bottom water becomes hypoxic during the summertime (Rabalais et al. 2002).

1.3 Model Specification

1.3.1 Modeling Period and Data

The simulation covered June 1–June 30, 2009, with several days of spin up in May because the summer-related thermal stratification usually starts in June (Allahdadi et al. 2013). Field measurements of the required Metocean data (current speed, wind speed, sea surface temperature, air temperature, air pressure) were available for June 2009 from the WAVCIS (www.wavcis.lsu.edu) station CSI-6, located off Terrebonne at 20 m water depth. The data were used for model setup and validation. Meteorological measurements, including air pressure, air temperature, wind speed, and relative humidity, as well as oceanographic data and sea surface temperature (SST), were used in calculating different components of input heat flux to the model (see Sect. 1.3.2.1). SST data are also used to compare with the simulated SSTs.

SST observed at CSI-6 increased from May to the maximum value in August and decreased thereafter (Fig. 1.2). SST values for a longer time period from May to December are shown in the inset of Fig. 1.2. The time series of June through July SST shows a generally increasing trend with an average initial SST value of about 26 °C during the first 5 days. SST increased to a maximum of 31 °C by June 20 with daily fluctuations of ~0.9 °C. SST variations during this time period (from June 10 to 20) are all oscillatory, presumably due to diurnal variation of heat flux, and these continued till mid-July, when diurnal fluctuations of SST almost

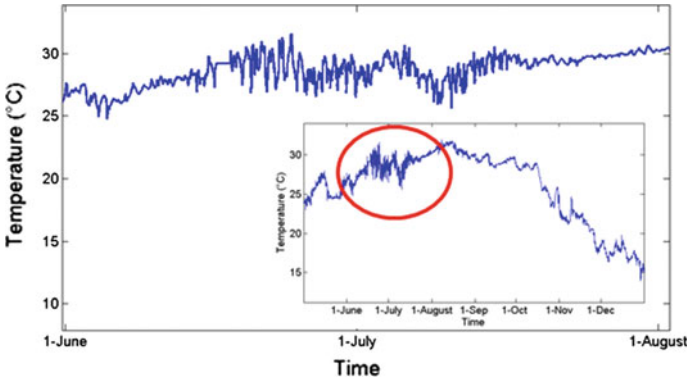

Fig. 1.2 Time series of measured SST at WAVCIS station CSI-6

disappeared and SST showed a gradual (almost smooth) increase. The nighttime mitigation of SST, and thereby reduced stratification that could contribute to re-oxygenation in the water column, was absent after mid-July and therefore more severe hypoxic events are expected.

1.3.2 Model Inputs

1.3.2.1 Heat Flux

The effect of solar insolation on water temperature and density was incorporated into the FVCOM model through two components of the surface boundary condition: net surface heat flux and short wave radiation flux. Although these parameters can be obtained from atmospheric model databases, low temporal resolution of the available model outputs (time steps of 6 h or larger) limits their use for a detailed study of diurnal shelf heating and stratification. Hence, the two heat flux components were calculated using hourly Metocean data.

Net surface heat flux is the algebraic sum of four different components:

$$Q_N = Q_s + Q_{LW} + Q_L + Q_{sn} \tag{1.5}$$

where the quantities in the right-hand side of the equation are shortwave, longwave, latent heat, and sensible heat fluxes, respectively. For each of them, the equations are presented in Appendix A.

The hourly Metocean data used for the calculation of heat flux components provided an adequate temporal resolution of shortwave radiation and net heat flux. Following the approach presented in Appendix A and using Eq. 1.5, we calculated shortwave radiation and net heat flux for the simulation period using the Metocean data from CSI-6 (Fig. 1.3). The peak values show the daytime maximum insolation

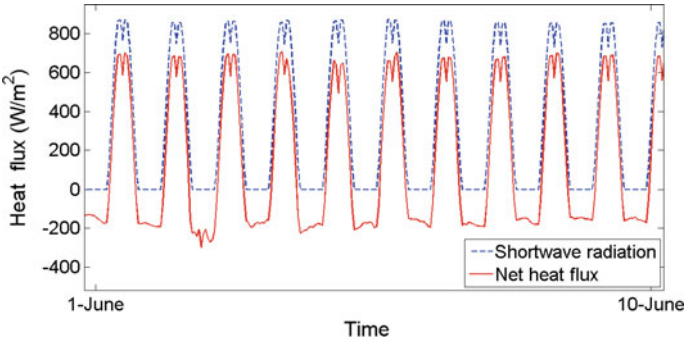

Fig. 1.3 Variation in calculated shortwave radiation and net surface heat flux for June 1–June 10, 2009

occurring two times between 1 and 4 PM. The two distinct peaks of heat flux correspond to two maxima of the function for cosine of the zenith angle used in the calculation (Appendix A).

Shortwave radiation is the only component of net heat flux that penetrates through the water column. Attenuation of shortwave flux versus water depth is presented by the following equation (Chen et al. 2003):

$$SW(z,t) = SW(0,t)\left[Re^{\frac{z}{a}} + (1-R)e^{\frac{z}{b}}\right] \tag{1.6}$$

where $SW(0,t)$ is the shortwave radiation at the water surface, t is time, and $SW(z,t)$ is the shortwave radiation at water depth z. Parameters a and b are the attenuation lengths for longer and shorter (waveband blue-green) wavelengths, and R is the portion of shortwave flux associated with the longer wavelengths. Appropriate values for a, b, and R should be considered based on the clarity of water over the modeling area. Paulson and Simpson (1977) suggested values of R = 0.78, $a = 1.4$, and $b = 7.9$ for coastal waters. In our study, a sensitivity analysis was implemented on each parameter to obtain the optimal agreement with SST measurements. The final applied values were consistent with Chen et al. (2003).

1.3.2.2 Wind Data

We considered the effect of wind, and the associated mixing, in order to evaluate the model performance and to properly interpret the effects of solar heating on stratification. Wind data for June 2009 were obtained from CSI-6 and reduced to the standard level of 10 m above sea surface. The average wind speed during this month was less than 6 m/s and rarely reached 10 m/s (Fig. 1.4). This implies a weak wind effect on mixing over the shelf.

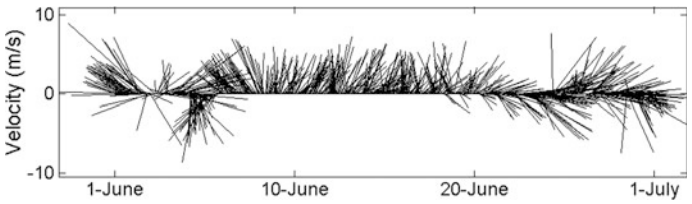

Fig. 1.4 Time series of wind speed measurements at station CSI-6 for June 2009

1.3.2.3 Initial Temperature Profile

We used the climatological profile for May over the Louisiana shelf from NOAA as the initial temperature profile for FVCOM. Site-specific measurements were not sufficient to obtain temperature profiles for the initial conditions.

1.3.3 Boundary Conditions

A dissipative internal boundary condition was used to damp the waves reflected from the boundary to the model domain. No temperature or salinity values were applied to the open boundary, and also no tide was assumed at the boundary.

1.4 Simulation Results

1.4.1 Model Evaluation

Simulated currents under wind forcing were compared with available measurements at WAVCIS stations CSI-6 and CSI-9 (Fig. 1.5, see Fig. 1.1 for locations). Small values of simulated currents for this time period are consistent with measurements and previous studies (Allahdadi et al. 2013; Chaichitehrani et al. 2014) Current measurements during simulation period were available for only several days. Results for SST were compared to field measurements at CSI-6 (Fig. 1.6a). An optimal agreement was achieved for the case that used the short/longwave attenuation lengths suggested by Chen et al. (2003). FVCOM reproduced the increasing SST trend from 26.5 to 30 °C for June 3–June 15.

Simulated daily fluctuations of temperature are more or less in phase with measurements showing the mid-day temperature peak and nighttime minimum (Fig. 1.6a). The simulated time series of SST was de-trended to show the fluctuations associated with diurnal variations of solar insolation. The resultant time series of daily temperature fluctuations (Fig. 1.6b) show a maximum day–night temperature difference of 0.9 °C with an average of 0.5 °C for the first 20 days of June 2009.

1.4.2 Sea Surface Temperature

Simulated spatial variation of SST was complicated due to complex shelf bathymetry and the dynamics of circulation on the shelf (Fig. 1.7). SST maps of the study area for different times on July 15 show the effects of including the minimum

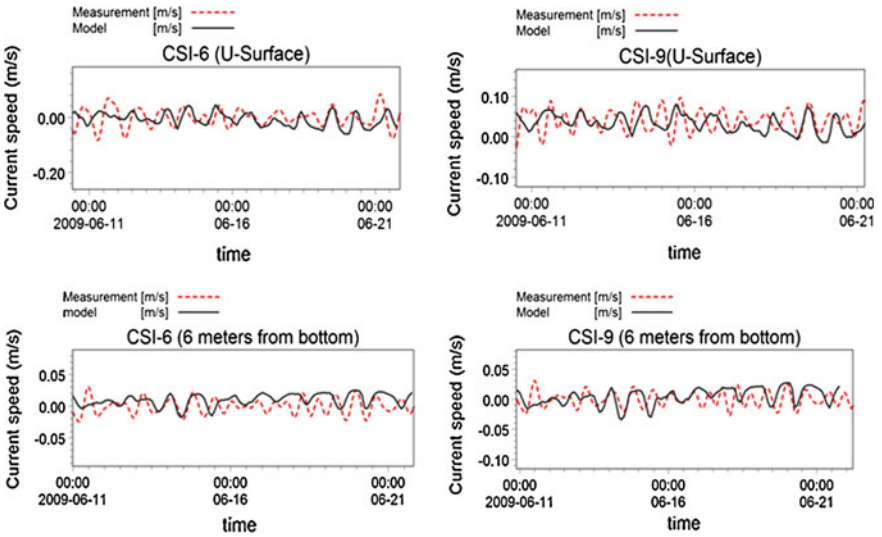

Fig. 1.5 Comparison of measured and simulated east–west current component (U-component) for surface and bottom at stations CSI-6 and CSI-9

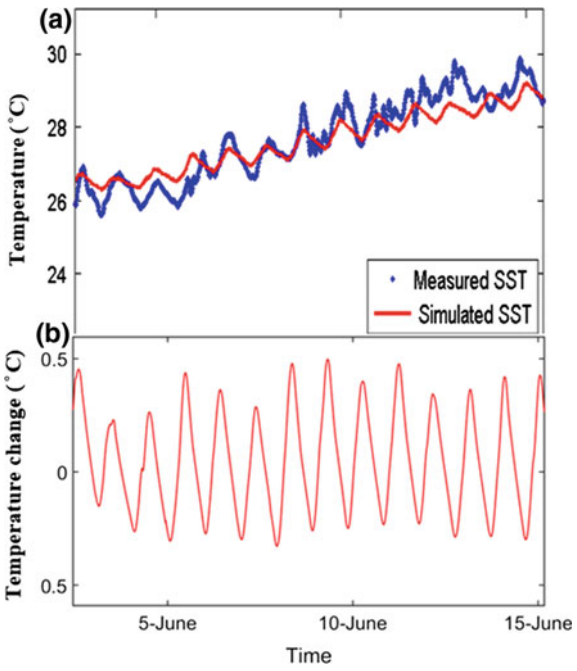

Fig. 1.6 **a** Comparison of simulated and measured SST at station CSI-6; **b** day–night fluctuations in SST

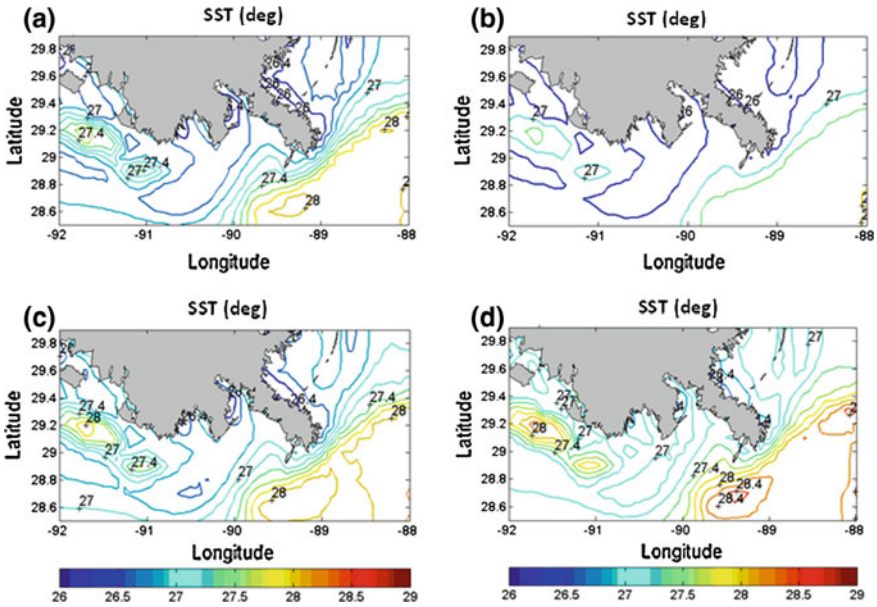

Fig. 1.7 Shelf-wide variation in simulated SST for June 15, 2009; **a** 12:00 AM, **b** 3:00 AM, **c** 12:00 PM, and **d** 3:00 PM

nighttime radiation and peak daytime radiation. Shelf-wide SST map at 12:00 AM local time (Fig. 1.7a) shows that simulated SST over the shelf area off the Barataria and Terrebonne Bays was uniform at about 26.5 °C. Over the shallow shelf off the Atchafalaya Bay, SST was higher (27.4 °C), which can be partly due to the smaller depths and advection of warm water from outer-shelf to this area. SST over the deep waters off the Mississippi Delta was higher (28 °C) compared to the inner-shelf waters. Three hours later at 3:00 AM (Fig. 1.7b), which is several hours after the intense daytime solar insolation, SST distribution off the Barataria and Terrebonne bays was similar to the values at 12:00 AM, but SST off the Atchafalaya Bay and the Mississippi Delta decreased to about 27 and 27.1 °C, respectively. At 12:00 PM (Fig. 1.7c), the daytime increase of solar insolation caused SST to increase off the Atchafalaya Bay to about 28 °C and off the Mississippi Delta to about 28.2 °C. Temperature distribution over the shelf just west of the Mississippi Delta was similar to other two time steps (12:00 AM and 3:00 AM), but with temperature increased to about 26.8 °C. Corresponding to the peak of insolation at 3:00 PM (Fig. 1.7d), SST over the shelf west of the Mississippi Delta increased to 27–27.2 °C and similarly increased in other areas over the shelf.

1.4.3 Vertical Distribution of Temperature

The simulated increase in SST as a result of solar insolation affected the development of temperature stratification. Furthermore, the temperature difference during daytime and nighttime produced diurnal differences in water column stratification. The general behavior of induced shelf stratification based on simulation results is presented along an east–west cross section (Sect. 1.1 in Fig. 1.1). The section extends from the southwest Pass to Sabine Bank that is about 400 km west of the Mississippi Delta and represents the vertical variation in simulated temperature for the inner-shelf region. Figure 1.8 shows the depth profiles of temperature across this section for two different times (12:00 AM and 3:00 PM) on June 15 (almost 15 days after the SST started to increase). Solar heating induced stratification along the initially mixed shelf, except for a shallow region of 30–50 km width (water depth less than 10 ms) located west of the Terrebonne Bay over which the water column was well mixed (Fig. 1.8a). However, the upper part of the water column (upper 7 m) for all points along the section remained well mixed. Water temperature increased from the initial value of 25 °C to highest value of about 27 °C just west of the Mississippi Delta off Barataria Bay, as well as over the shallow and well-mixed region west of the Terrebonne Bay. As compared to 12:00 AM, the 3:00 PM profiles occurred at the peak daytime SST values of 28 °C (Fig. 1.8b). This peak followed the maxima in solar insolation and was associated with a much stronger stratification compared to nighttime (12:00 AM) values. At other time points during the simulation period, the daytime and nighttime stratification patterns were similar to daytime and nighttime patters as shown in Fig. 1.8. Temperature distribution at depths greater than 10 m remained unchanged from day to night, consistent with the attenuating effect of water column depth on short wavelength radiation. Throughout the simulation period, isotherms were tilted upward in the shelf area between the Terrebonne and Barataria bays in response to upwelling resulting from the southwesterly winds.

The diurnal evolution of water column stratification is illustrated with vertical profiles on transect A (Fig. 1.9) on the shelf in front of the Terrebonne Bay (see Fig. 1.1 for location). Water temperatures are shown at four different times on June 15 for the shelf waters up to 50 m. At night (Fig. 1.9a), the mixed layer depth for the shoreward region of the transect (depths smaller than 20 m) was 7–10 m, while the SST was about 26.3 °C. For the deeper region, the mixed layer depth was shallower (less than 5 m) and SST was about 27 °C. Three hours later at 3:00 AM (Fig. 1.9b), the overall pattern of temperature distributions in both shallower and deeper water was similar. However, the mixed layer depth in the shallower region decreased to about 5 m or less, and the associated SST increased to 26.6 °C. At 12:00 PM (Fig. 1.9c), when there was a substantial increase in solar radiation compared to that of morning time over the major part of the shallow shelf, isotherms shifted upward making mixed layer depths less than 5 m. SST over the shallow area increased to 26.9 °C, while the deeper locations had SST values of about 27 °C. The strongest stratification occurred at 3:00 PM (Fig. 1.9d) and

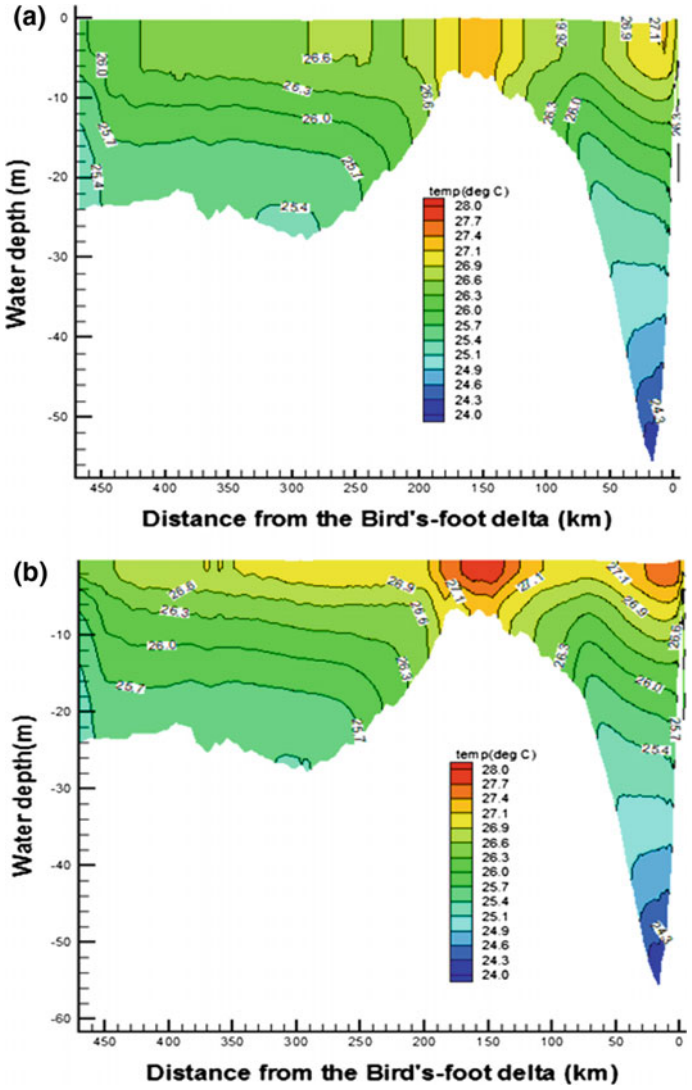

Fig. 1.8 Simulated **a** nighttime and **b** daytime temperature distributions along east–west transect (Sect. 1.1 in Fig. 1.1) for June 15, 2009

extended across the entire transect length with SST increased to 27 °C. Isotherms were closer to each other compared to other times, demonstrating larger vertical temperature gradient and stronger stratification at 3:00 PM compared to the other times.

Development of stratification during night and daytimes is also illustrated using temperature profiles along transect B west of the Mississippi Delta in front of the

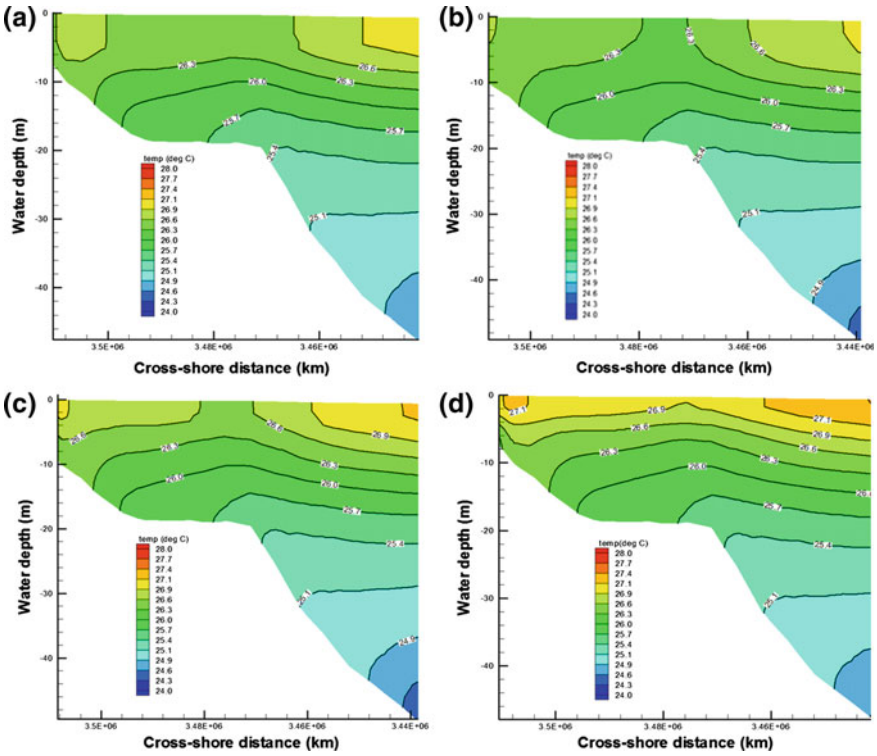

Fig. 1.9 Simulated changes in stratification along transect A for June 15, 2009; **a** 12:00 AM, **b** 3:00 AM, **c** 12:00 PM, and **d** 3:00 PM

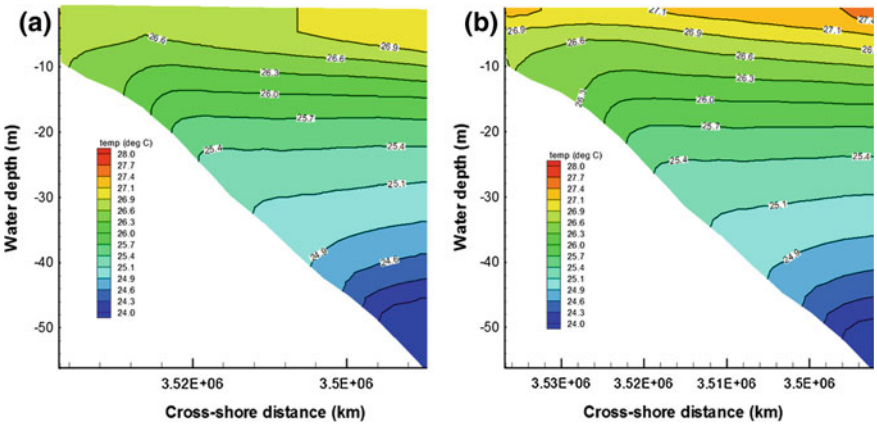

Fig. 1.10 Simulated temperature values across transect B on July 15, 2009; **a** 12:00 AM and **b** 3:00 PM

Barataria Bay (Fig. 1.10). This transect extends to around 60-m depth over an area with a steeper bed slope compared to transect A. The difference between the thermal stratification for night and day was more or less similar to that of transect A. At 12:00 AM on June 15, a well-established stratified layer developed beneath the mixing depth of 5–10 m and SST was 26.9–27 °C (Fig. 1.10a). Also similar to transect A, at 3:00 PM (Fig. 1.10b), the daytime stratification was stronger compared to nighttime.

1.5 Representing Stratification Based on Gradient Richardson Number

The vertical temperature distribution along east–west and cross-shore transects qualitatively showed that the strength of stratification increased on both diurnal and monthly timescales. In order to quantify this conclusion, buoyancy frequency and gradient Richardson number were examined. Richardson number is defined as the ratio of buoyancy to the shear forces in the water column (Lyons et al. 1964):

$$R_i = \frac{N^2}{\left(\frac{\partial u}{\partial z}\right)^2 + \left(\frac{\partial v}{\partial z}\right)^2} \tag{1.7}$$

$$N^2 = -\frac{g}{\rho_0}\frac{\partial \rho}{\partial z} \tag{1.8}$$

in which u and v are the horizontal velocity components varying in the vertical (z) direction, ρ is water density, and g is gravitational acceleration (m/s^2). The quantity N^2 is the Brunt-Väisälä or buoyancy frequency. If the Richardson number is larger than 1, then buoyancy forces outweigh shear forces; hence, the water column is stable. If the Richardson number is smaller than 0.25, then shear and turbulence forces dominate and the water column is unstable, which leads to vertical mixing (Lyons et al. 1964; Turner 1973; Galperin et al. 2007).

Variation of temperature in the water column causes density to change and thereby changes buoyancy frequency. Since SST oscillates diurnally, similar variation for surface water density and the gradient Richardson number across the water column are also expected. Figure 1.11a shows the results for time variation of water density at the surface and mid-depth (depth of 10 m from the surface) at the location of CSI-6. The surface and mid-depth locations were selected to calculate the Richardson Number. The decreasing trend of density is consistent with increasing trend of water temperature during the simulation period. Surface water density follows a similar diurnal pattern as SST. No fluctuations were present for water density at the 10-m depth (mid-water). During the nighttime between June 5 and June 10, surface water density increased to about the mid-depth density due to the nighttime minimum heating. However, after June 10, the difference in densities

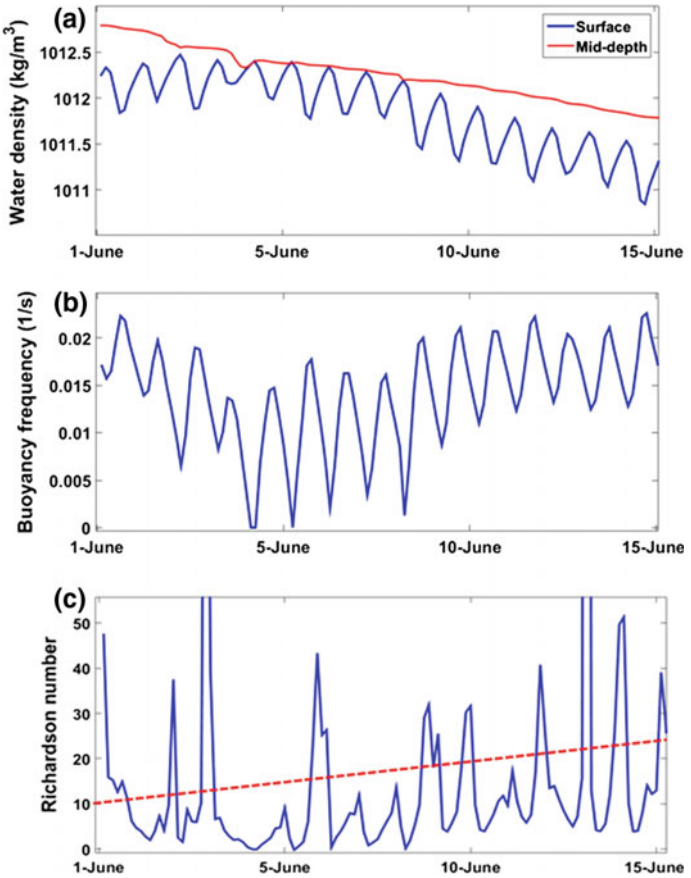

Fig. 1.11 Temporal changes in **a** simulated water density, **b** calculated buoyancy frequency, and **c** calculated Richardson number during June 1–15, 2009, of the simulation. *Dashed line* in Fig. c. denotes the temporal trend in Richardson numbers

increased as a result of faster heating of the surface water compared to the mid-water. Note that the mid-depth density experienced a drop caused by the mixing event of 4 June.

Vertical gradient of water density at the same location was quantified to obtain buoyancy frequency (Fig. 1.11b). The variation over time in buoyancy frequency was similar to SST and surface density on both monthly and diurnal scales. Before June 5, buoyancy frequency experienced a general declining trend caused by a northern wind-induced mixing. After this date, buoyancy effect increased as shelf waters were exposed to higher solar heating.

The strength of stratification was quantified based on the gradient Richardson number at a fixed point, which is the mid-depth water at CSI-6 location (water depth of 10 m). Vertical gradients of current components at the mid-depth were

calculated based on the results for wind-induced currents. Since wind speed at the time was generally weak (less than 7 m/s), its impact on mixing was small. The resultant Richardson number was therefore large, showing the dominant effect of buoyancy. The time variation of Richardson number in the mid-depth waters at CSI-6 showed an increasing trend (Fig. 1.11c). The small values of Richardson number prior to June 5 show the effect of wind mixing events. Variations of buoyancy frequency and Richardson number elsewhere over the shelf were similar.

1.6 Diurnal Heating/Stratification and Measured Bottom Oxygen Concentration

Our simulation results showed that stratification becomes stronger as a result of summertime solar insolation. Hence, it is expected that bottom water oxygen concentration would decrease during June 2009 as a stratified water column blocked water re-oxygenation. Time series of measured oxygen concentrations at the bottom of CSI-6 (Fig. 1.12a) during June 2009 verified this. Oxygen concentration was about 4 mg/l on the first day of June 2009, followed by a decline, presumably due to increasing solar radiation and the consequent stratification as well as enhanced biological processes. On June 4, the northerly winds increased

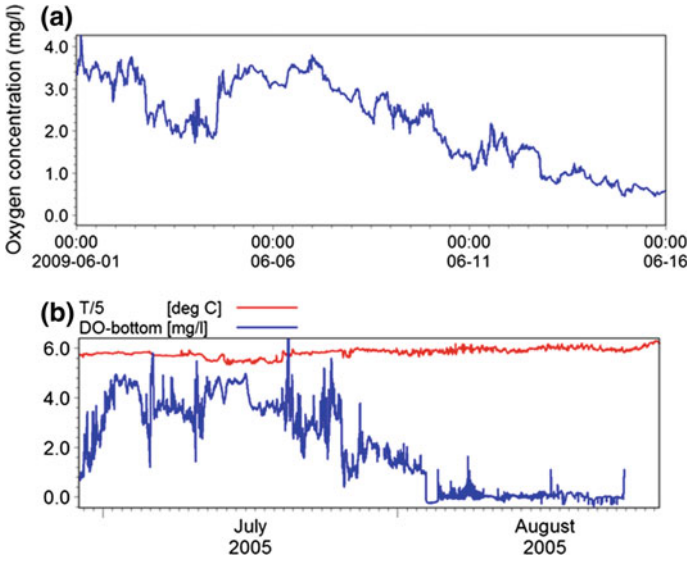

Fig. 1.12 **a** Measured bottom water oxygen concentration at station CSI-6 for June 1–June 15, 2009. **b** Measured SST and bottom water oxygen concentration for July and August 2005

oxygen concentration from 2 mg/l to about 4 mg/l. After this, with the reinforcement of stratification (see Fig. 1.11), oxygen concentration started a longer term decline, depleting the bottom oxygen to less than 1 mg/l. Declining measured bottom oxygen concentrations were consistent with the increase in the simulated SST and the associated buoyancy frequency (implying that the wind-induced mixing was not significant). The consistency was also examined for measurements of dissolved oxygen at CSI-6 during the summer of 2005 (Fig. 1.12b). Time series of bottom oxygen concentration during July 2005 had an average of 4 mg/l for the first 20 days when the average SST was 29 °C. During the next two weeks, SST increased to greater than 30 °C, coincided with declining oxygen concentration. Oxygen concentration then decreased from 4 mg/l to about 1.6 mg/l between July 20 and August 3 when SST increased to 31 °C. This hypoxic bottom water persisted on the shelf until the middle of the last week of August 2005, when mixing produced by Hurricane Katrina broke down the stratification and re-oxygenated the bottom water.

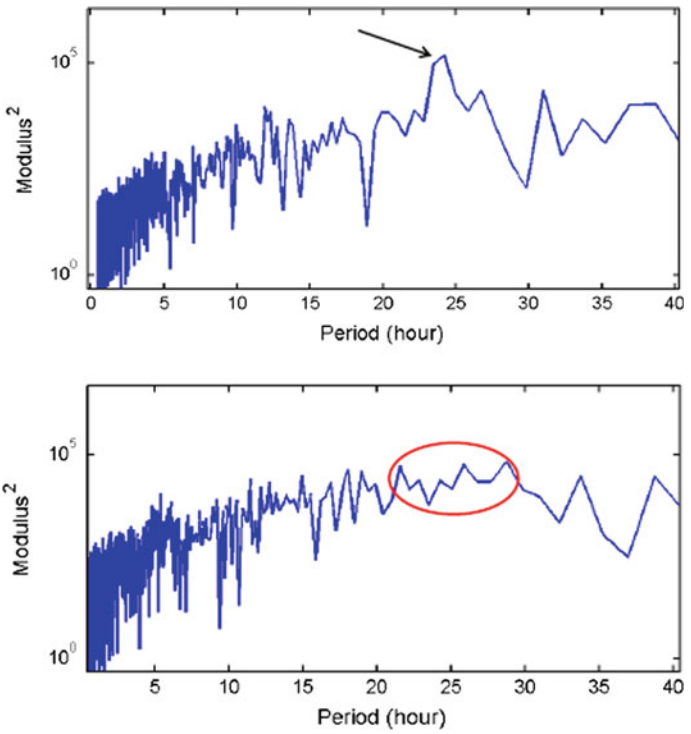

Fig. 1.13 *Upper panel,* energy spectrum of measured SST at station CSI-6 during summer 2005. The *arrow* shows the daily dominant spectral energy for this parameter. *Lower panel,* the corresponding energy spectrum for measured bottom oxygen concentration at station CSI-6. The dominant range of spectral energy is denoted by an *ellipse*

The coincident variation of SST (which is mainly produced by solar heating) and bottom water oxygen concentration are further elaborated by examining the energy spectrum of each parameter during the measurement period of July and August 2005 (Fig. 1.13). The peak of energy for SST was daily (24 h), and bottom oxygen concentration peaked within a narrow band from 22 to 28 h. This accounts for the strong daily variation in bottom oxygen concentration. Based on these time series comparisons, diurnal heating of water column and the resulted stratification can be a main contributor. However, it should be noted that strengthening stratification is not the only effect of the heating induced by solar radiation. Enhanced biological process as a result of higher water temperature can significantly contribute to the oxygen depletion of bottom water. The present study did not address the oxygen consumption by biological processes, and our main focus was demonstrating the role of diurnal solar heating during summertime as a barrier for re-oxygenation from the water surface.

1.7 Summary and Conclusion

Development of daily stratification, caused by summertime increases in solar radiation over Louisiana shelf, was studied using the 3-D FVCOM circulation model. SST over the shelf west of the Mississippi Delta increased from 25 °C on June 1, 2009, to about 28.5 °C on June 20, 2009. In addition to the diurnal variation of solar radiation, SST increased steadily during the month. Model simulation showed that the steady increase in the temperature of the surface layer caused the enhancement of stratification. As a result, the stratification was widespread on the shelf west of the Mississippi Delta and was stronger during the daytime and weaker during the nighttime. The stratification developed more over the shelf area off the Terrebonne Bay to the Mississippi Delta. This is the area that historically has had the most severe hypoxic events.

Analysis showed that the buoyancy frequency followed the same increasing trend of SST in the absence of significant mixing. The Richardson number exhibited an increase after the initial mixing over the shelf. Stratification was consistent with the measured bottom water dissolved oxygen during the simulation period. Oxygen concentration decreased with the increasing SST and stratification strength during period with little mixing.

Acknowledgements The authors are grateful to Nancy Rabalais for sharing the dissolved oxygen data from WAVCIS-CSI-6 and Changsheng Chen for providing the FVCOM.

Appendix A: Formulation of Different Surface Heat Components

(All parameters are described in Table 1.1)

Shortwave Radiation: Relationships presented by Guttman and Matthews (1979), Ivanoff (1977), and Cotton (1979) were used to calculate shortwave radiation flux:

$$Q_o = \frac{Scos^2 Z}{(\cos Z + 2.7)e \times 10^{-5} + 1.085 \cos Z + 0.10} \tag{1.9}$$

The cosine of the zenith angle is computed using the formula:

$$\cos Z = \sin\phi \sin\delta + \cos\phi \cos\delta \cos HA \tag{1.10}$$

Table 1.1 Parameters used for the formulation of surface heat components

Variable	Value	Description
(a, b)	(9.5, 7.66)	Vapor pressure constants over ice
(a, b)	(7.5, 35.86)	Vapor pressure constants over water
C		Cloud cover fraction
C_E	1.75×10^{-3}	Transfer coefficient for latent heat
C_H	1.75×10^{-3}	Transfer coefficient for sensible heat
c_p	1004 J kg^{-1} K^{-1}	Specific heat of dry air
Δ		Declination
E		Vapor pressure in pascals
e_s		Saturation vapor pressure
$\in$	0.622	Ratio of molecular weight of water to dry air
HA		Hour angle
L	2.5×10^6 J kg^{-1}	Latent heat of vaporization
L	2.834×10^6 J kg^{-1}	Latent heat of sublimation
Φ		Latitude
$Q_\circ$		Incoming radiation for cloudless skies
q_s		Surface specific humidity
q_{10m}		10 m specific humidity
ρ_a		Air density
S	1353 W m^{-2}	Solar constant
Σ	5.67×10^{-8} W m^{-2} K^{-4}	Stefan–Boltzmann constant
T_a		Air temperature
T_d		Dew point temperature
T_{sfc}		Surface temperature of the water/ice/snow
V_{wg}		Geostrophic wind speed
Z		Solar zenith angle

The declination is $\delta = 23.44^{\circ} \times \cos\left[(172 - day\ of\ year) \times 2\pi/365\right]$, and the hour angle is $HA = (12\,h - solar\ time) \times \pi/12$. The correction for cloudiness is given by

$$SW\downarrow = Q_o(1 - 0.6c^3) \tag{1.11}$$

The cloud correction is optional since some sources of radiation contain it already.

Longwave Radiation: The clear sky formula for incoming longwave radiation is given by Wyrtki (1965):

$$F\downarrow = \sigma T_a^4 \left\{1 - 0.261 \exp\left[-7.77 \times 10^{-4}(273 - T_a)^2\right]\right\} \tag{1.12}$$

while the cloud correction is given by:

$$LW\downarrow = (1 + 0.275c)F\downarrow \tag{1.13}$$

Sensible Heat: The sensible heat is given by the standard aerodynamic formula (Imberger and Patterson 1981):

$$H\downarrow = \rho_a c_p C_H V_{wg}\left(T_{a-} T_{sfc}\right) \tag{1.14}$$

Latent Heat: The latent heat depends on the vapor pressure, and the saturation vapor pressure given by Imberger and Patterson (1981):

$$e = 611 \times 10^{a(T_d - 273.16)/(T_d - b)} \tag{1.15}$$

$$e_s = 611 \times 10^{a(T_{efc} - 273.16)/(T_{efc} - b)} \tag{1.16}$$

The vapor pressures are used to compute specific humidity according to:

$$q_{10m} = \frac{\in e}{p - (1 - \in)e} \tag{1.17}$$

$$q_s = \frac{\in e_s}{p - (1 - \in)e_s} \tag{1.18}$$

The latent heat is also given by a standard aerodynamic formula:

$$LE\downarrow = \rho_a L C_E V_{wg}(q_{10m} - q_s) \tag{1.19}$$

References

Allahdadi M (2015) Numerical experiments of hurricane impact on vertical mixing and re-stratification of the Louisiana shelf. Baton Rouge, Louisiana, Louisiana State University, PhD dissertation, 178p

Allahdadi MN, Jose F, Patin C (2013) Seasonal hydrodynamics along the Louisiana coast: implications for hypoxia spreading. J Coastal Res 29:1092–1100

Bender MA, Ginis I, Kurihara Y (1993) Numerical simulations of tropical cyclone-ocean interaction with a high-resolution coupled model. J Geophys Res-Atmos 98:23245–23263

Chaichitehrani N (2012) Investigation of colored dissolved organic matter and dissolved organic carbon using combination of ocean color data and numerical model in the Northern Gulf of Mexico. Baton Rouge, Louisiana, Louisiana State University, Master's thesis, 112p

Chaichitehrani N, D'Sa EJ, Ko DS, Walker ND, Osburn CL, Chen RF (2014) Colored dissolved organic matter dynamics in the Northern Gulf of Mexico from ocean color and numerical model results. J Coastal Res 30(4):800–814

Chen C, Cowles G, Beardsley RC (2006) An unstructured grid, finite volume coastal ocean model: FVCOM user manual, 2nd edn. SMAST/UMASSD Technical Report-06-0602, p 315

Chen CS, Beardsley RC, Franks PJS, Van Keuren J (2003) Influence of diurnal heating on stratification and residual circulation of Georges Bank. J Geophys Res-Oceans 108

Cotton GF (1979) ARL models of global solar radiation. In: Quinlan FT (ed) SOLMET volume 2: hourly solar radiation—surface meteorological observations. National Oceanic and Atmospheric Administration, Asheville, NC, pp 165–184

Elsberry RL, Fraim TS, Trapell RN (1976) Mixed layer model of oceanic thermal response to hurricanes. J Geophys Res-Oceans Atmos 81:1153–1162

Galperin B, Sukoriansky S, Anderson PS (2007) On the critical Richardson number in stably stratified turbulence. Atmos Sci Lett 8:65–69

Guttman NB, Matthews JD (1979) Computation of extraterrestrial solar radiation, solar elevation angle and true solar time of sunrise and sunset. In: Quinlan FT (ed) SOLMET volume 2: hourly solar radiation—surface meteorological observations. National Climatic Center, US Department of Commerce, Asheville, NC, pp 48–54

Hagy JD, Murrell MC (2007) Susceptibility of a Northern Gulf of Mexico estuary to hypoxia: an analysis using box models. Estuar Coast Shelf Sci 74:239–253

Imberger J, Patterson JC (1981) A dynamic reservoir simulation model—DYRESM: 5. In: Fischer HB (ed) Transport models for inland and coastal waters. Academic Press, pp 310–361

Ivanoff A (1977) Oceanic absorption of solar energy. In: Kraus EB (ed) Modelling and prediction of the upper layers of the ocean. Pergamon, New York, p 326

Justic D, Rabalais NN, Turber RE (2003) Simulated responses of the Gulf of Mexico hypoxia to variations in climate and anthropogenic nutrient loading. J Mar Syst 42:115–126

Justic D, Rabalais NN, Tutner RE (1996) Effects of climate change on hypoxia in coastal waters: a doubled CO2 scenario for the Northern Gulf of Mexico. Limnol Oceanogr 41:992–1003

Lyons R, Panofsky HA, Wollaston S (1964) The critical Richardson number and its implication for forecast problems. J Appl Meteorol 3:136–142

Nezlin NP, Kamer K, Hyde J, Stein ED (2009) Dissolved oxygen dynamics in a eutrophic estuary, Upper Newport Bay, California. Estuar Coast Shelf Sci 82:139–151

Paulson CA, Simpson JJ (1977) Irradiance measurements in the upper ocean. J Phys Oceanogr 7:952–956

Price JF (1981) Upper ocean response to a hurricane. J Phys Oceanogr 11:153–175

Rabalais NN, Atilla N, Normandeau C, Turner RE (2004) Ecosystem history of the Mississippi river-influenced continental shelf revealed through preserved phytoplankton pigments. Mar Pollut Bull 49:537–547

Rabalais NN, Turner RE, Scavia D (2002) Beyond science into policy: Gulf of Mexico hypoxia and the Mississippi River. Bioscience 52:129–142

Rabalais NN, Louisiana Universities Marine Consortum (1991) Fate and effects of nearshore discharges of OCS produced waters New Orleans (1201 Elmwood Park Boulevard, New Orleans 70123-2394), U. S. Dept. of the Interior, Minerals Management Service, Gulf of Mexico OCS Regional Office

Tehrani NC, D'Sa EJ, Osburn CL, Bianchi TS, Schaeffer B (2013) A chromophoric dissolved organic matter and dissolved organic carbon from sea-viewing wide field-of-view sensor (SeaWiFS), Moderate resolution imaging spectroradiometer (MODIS) and MERIS sensors: case study for the Northern Gulf of Mexico. Remote Sens 5:1439–1464

Turner RE, Rabalais NN, Justic D (2008) Gulf of Mexico hypoxia: alternate states and a legacy. Environ Sci Technol 42:2323–2327

Turner RE, Rabalais NN (1994) Coastal eutrophication near the Mississippi river delta. Nature 368:619–621

Turner JS (1973) Buoyancy effects in fluids. Cambridge University Press, London, Cambridge

Wang LX, Justic D (2009) A modeling study of the physical processes affecting the development of seasonal hypoxia over the inner Louisiana-Texas shelf: circulation and stratification. Cont Shelf Res 29:1464–1476

Wiseman WJ, Rabalais NN, Turner RE, Dinnel SP, Macnaughton A (1997) Seasonal and interannual variability within the Louisiana coastal current: stratification and hypoxia. J Mar Syst 12:237–248

Wyrtki K (1965) The average annual heat balance of the North Pacific ocean and its relation to ocean circulation. J Geophys Res 70(18):4547–4559

Zedler SE, Dickey TD, Doney SC, Price JF, YU X, Mellor GL (2002) Analyses and simulations of the upper ocean's response to Hurricane Felix at the Bermuda Testbed Mooring site: 13–23 August 1995. J Geophys Res-Oceans 107